DUAL-SIDE CHANNEL SPR BASED PHOTONIC CRYSTAL FIBER SENSOR

وَمَن يُؤْتَ الْحِكْمَةَ
فَقَدْ أُوتِيَ خَيْرًا كَثِيرًا

QUAID-I-AZAM UNIVERSITY

ISLAMABAD

By

Abdul Muqeet

Department of Electronics

Faculty of Natural Sciences

Quaid-i-Azam University, Islamabad

2023

In the Name of Allah The Most Merciful and The Most Beneficent

Certificate

The undersigned hereby certify that they have read and recommend to the Faculty of Graduate Studies for acceptance a thesis entitled "Dual-Side Channel SPR based Photonic Crystal Fiber Sensor" by "Abdul Muqeet" in partial fulfillment of the requirements for the degree of Master of Philosophy.

Supervisor:

Dr. Muhammad Aqeel Ashraf

Professor

Department of Electronics,

Quaid-i-Azam University, Islamabad, Pakistan

Chairman:

Dr. Qaisar Abbas Naqvi

Professor

Department of Electronics,

Quaid-i-Azam University, Islamabad, Pakistan

Dedication

I am feeling great honor and pleasure to dedicate this research work to

My Mother

Whose prayers and wishes have been a great source of comfort for me during my whole life

Acknowledgments

In the name of Almighty Allah, the Merciful, the Beneficent All praises (belong) to Allah alone, the Cherisher and Sustainer of the world. He is the First, he is the Last, He is the Hidden and He knows about everything. He brings the night into the day and brings the day into the night and He knows the thoughts of hearts. (Al-Quran)

I offer my humble veneration and gratitude to my father Prof. M. Maqbool, for their financial and moral support, my nephew Haider Karrar and my loving brothers Armaghan Ahmad and M. Wasiq who always remembered me in their prayers and wishes.

ABDUL MUQEET

14-12-2023

Abstract

A novel dual-core photonic crystal fiber (PCF) sensor is designed to mimic visible and near-infrared regimes through the utilization of surface plasmon resonance (SPR). The sensor design aims to achieve wide refractive index (RI) sensing capabilities and simultaneous detection of multiple analytes. The PCF design features two concentric rings forming the cladding in a circular lattice configuration, strategically omitting air holes on both sides adjacent to the metal layer to enhance coupling effects. To induce plasmon resonance, a chemically inert thin layer of gold is applied to the half-ellipse shaped sensing channels. Utilizing the finite element method in COMSOL Multiphysics, we systematically explore the optical characteristics of suggested SPR based PCF. Operating within visible band, sensor demonstrates the ability to simultaneously detect multiple analytes within the range of 1.35-1.44. Furthermore, it exhibits a wider RI sensing range from 1.15 to 1.44 in the near-infrared(n-IR) band. The sensor showcases a wavelength sensitivity of 1840 nm/RIU and an amplitude sensitivity of 168.13 RIU^{-1} with a resolution of 6.71×10^{-5} RIU in the n-IR band. Conversely, in visible band, the sensor demonstrates higher sensitivity, reaching up to 4520 nm/RIU, and an amplitude sensitivity of 1093.29 RIU^{-1} with a resolution of 5.43×10^{-5} RIU. These findings underscore the potential of the dual-core SPR based PCF sensor for versatile and high-performance applications in RI sensing and multi-analyte detection for visible and near-infrared spectroscopy.

Contents

Chapter 1

Introduction

In the modern era, sensing is very important for industrial and scientific applications of advanced technologies. Sensors play a significant role in our daily lives. Sensors are used to raise safety standards and increase quality of life. Optical sensing systems have gained a lot of attention in sensing applications. Optical sensing is rapid due to the nature of light, highly precise, lightweight, and smaller in size. Optical sensing is a growing field and related to different branches of engineering. Optical sensors are based on light-matter interaction where electromagnetic fields vary due to presence of analyte to be detected. The working principles of optical sensors are refractive index(RI), fluorescence, reflectance, luminescence, and absorbance. A very small variation of refractive index can be sensed by surface plasmon resonance sensor (SPR). That is why, SPR is used extensively to detect and measure the physical quantities that cause the change in refractive index. Food safety[1], biomedicine[2], petrochemical industry[3], and environmental pollution[4] are the fields in which SPR has widespread implications. The advantages of fiber-optic sensors are small size, non-electrical devices, remote sensing, immune to EMI and RFI, non-corrosive, multiple environmental parameters sensing, less weight and small cables, remote sensing, pollution-free, high resolution, high sensitivity and dynamic range[5].

On the basis of coupling of light, SPR biosensors are divided into 4 types[6]. Photonic crystal fiber (PCF) and SPR combination(SPR-PCF) is very important and emerging technology in the field of sensing. SPR-PCF received attention because of its ability of remote sensing, small size, flexible design, and various other advantages[7]. Hassani and Skrobogity proposed the first SPR-PCF sensor in 2006[8]. PCFs have got attention in last few years due to exceptional light control ability and unique design. This unique property gives PCF several advantages over traditional fibers. These qualities enable the utilization of PCF in sensors[9],

multiplexers and demultiplexers[10], and polarization filters[11]. These holes create a patterned structure, known as a photonic crystal, which affects light propagation in fiber. Photonic crystal(PhC) is a periodic arrangement of dielectic material to alter the propagation characteristics. PhCs can be in one-dimensional arrangement or two-dimensional arrangement for their use in resonators, fibers and waveguide structures. For sensing purposes, one-dimensional is appropriate but it has poor light confinement[12]. Consistent one mode operation, less confinement loss, highly nonlinear behavior and high birefringence are some unique optical properties of PCF. Otto configuration and Kretschmann configuration are two configurations for the prism-based SPR sensor. Surface plasmons can be excited by the prism-coupled Kretschmann configuration but prism-coupled Kretschmann configuration is not suitable to remote and real time detection because of its large volume. These drawbacks have been overcome by SPR-PCF due to its small size[13]. Coupled mode theory is the basic principle on which SPR works. Any small change of analyte refractive index is visible as a resonant wavelength shift. Vapour deposition method is commonly used method of metal film coating[14]. To date, the proposed PCF designs have different types such as nanowire-based[15], internal metal-coated[16], slotted-based[17], D-shaped structures[18], and external metal-coated[19]. The air holes receive a targeted injection of the analyte in internal and nanowire-based sensing, and the plasmonic materials are positioned around the core. In reality, it can be challenging to carefully remove and fill air holes, and direct contact between metal surfaces and the core field causes significant propagation losses. Plasmonic materials, on the other hand, are externally coated in slotted-based and D-shaped configuration-based sensors. These sensors were problematic during practical application due to the necessity for precise surface polishing and spilling specifications, and the coating phenomenon is also a time-taking procedure. The extrinsic sensor is recommended for real-time environmental monitoring since it has the potential to address the shortcomings of the intrinsic sensor and other issues. The placement of metallic channel along the border of the PCF surface makes it simple to use this sensing technology. The recent widespread adoption of this approach for PCF-SPR sensing purposes is attributable to its straightforward and more useful detection capabilities[20].

The commonly used background material is silica because silica-based design has higher confinement losses while chalcogenide-based design has lower. The RI of other materials used is more than silica. So, the loss decreases because the light propagates in the material[21]. Plasmonic material is also a significant tuning parameter of SPR-PCF. Aluminum, copper, silver, and gold have been used in

SPR technology. The frequently used metals for SPR are silver and gold. Silver is not stable, but gold is a stable metal. That is why, gold is employed as metal in the suggested sensor.

In last decade, the predominant focus has centered on the detection of singular analytes using SPR sensors, with limited literature addressing sensors capable of concurrently detecting a diverse array of RIs and multiple analytes. Various researchers have proposed innovative designs of SPR-PCF sensors, each characterized by distinct RI detection ranges. Pan et al. [22] introduced an SPR-PCF sensor with a sensing range of RI spanning 1.26 to 1.38. Strategically placing gold in damaged air holes facilitated its role as the sensing channel for analytes. Simulation results exhibited a resolution of 1.78×10^{-5} RIU, and the maximum wavelength sensitivity (max-WS) achieved was 5626.86 nm/RIU. Haque et al. [23] devised a modified SPR-PCF tailored for detecting analytes within the range of RI fro, 1.18 to 1.36. The reported max-WS was 20,000 nm/RIU, with an amplitude sensitivity(AS) of 1054 RIU^{-1}, wavelength resolution of 5×10^{-6} RIU, and amplitude resolution of 16.7×10^{-6} RIU. Wang et al. [24] suggested an SPR-PCF capable of sensing RIs within the range of 1.13 to 1.35. Optimized parameters yielded a maximum sensitivity of 5.71×10^{-6} RIU and a resolution of 17,500 nm/RIU, evaluated within near-infrared(n-IR) spectrum from 0.865 to 1.675 µm. Zeng et al. [25] presented a sensor showcasing a max-WS of 12,600 nm/RIU and a maximum sensor resolution of 7.94×10^{-6} RIU within analyte RI range of 1.15 to 1.36. Two nanoscale gold belts served as the sensing channel on D-shaped PCF surface to achieve phase-matching conditions. Roni et al. [26] proposed a structural design proficient in sensing RIs within the range of 1.20 to 1.40. Gold strips on both sides enhanced the coupling process, resulting in a maximum amplitude sensitivity (max-AS) of 1277.47 RIU^{-1}, a WS of 5000 nm/RIU, and a resolution of 2×10^{-5} RIU. Xiao et al. [27] introduced a sensor tailored for RI sensing within range of 1.08-1.37, operating in the optical region of 1.210 to 2.140 µm. The design incorporated gold nanowires as a plasmonic metal to excite the SPR, achieving a max-WS of 13,000 nm/RIU. F. Haider et al. [28] reported a multi-analyte sensor utilizing an internal and external sensing approach, proficient in detecting analytes within 1.33 and 1.40, with a max-AS of 807 RIU^{-1}. Kamrunnahar et al. [29] suggested a sensor featuring two external channels for multi-analyte detection, operating within the RI range of 1.32-1.39, and achieving a max-AS of 928 RIU^{-1}. Mumtaz et al. [30] introduced a multi-analyte sensor designed for sensing RIs between 1.30 and 1.44, employing three external sensing channels. This windmill-shaped sensor exhibited a max-AS of -217 RIU^{-1}, a max-WS of 10,243 nm/RIU, and a figure of merit value

of 94.59 RIU^{-1}.

Basically, SPR-PCF function is based on evanescent field. The strong evanescent field can be gained by modulating the geometrical parameters of photonic crystal fiber[31]. In case of evanescent waves, operating wavelength is directly related to the skin depth. The evanescent wave's penetration depth is more in n-IR and mid-infrared bands than the visible light. That is why, the demand of sensors operating in the n-IR band and mid-infrared band has enhanced for ultra-wide RI sensing range[32]. Dual core is proposed in sensor because evanescent field decays exponentially. The aim while proposing a sensor is simple and cost effective design. The sensor proposed is good for detecting the dual-analyte simultaneously, analytes of low refractive indices, chemical analysis and bio-sensing.

Chapter 2

Photonic Crystal Fiber

A type of optical fiber called photonic crystal fiber (PCF), also referred to as micro-structured optical fiber, uses a periodic arrangement of tiny holes or voids throughout the fiber's length. These holes create a patterned structure, known as a photonic crystal, which affects light propagation in fiber. Photonic crystal(PhC) is a periodic arrangement of dielectric material to alter the propagation characteristics. PhCs can be in one-dimensional arrangement or two-dimensional arrangement for their use in resonators, fibers and waveguide structures. For sensing purposes, one-dimensional is appropriate but it has poor light confinement[12].

PCF has the cladding and core like conventional fiber but the difference is that cladding is made of air holes that run along the fiber. The propagation of waves can be managed by varying the size and position of holes. This unique property gives PCF several advantages over traditional fibers. The light propagating in PCF is either by modified total internal reflection(TIR) or photonic bandgap(PBG) effect. The advantages of PCF sensors over traditional fiber-based or prism sensors are robust, dense and cost-effective structure. Furthermore, the strong evanescent field can be gained by modulating the geometrical dimensions of photonic crystal fiber[31].

Any PCF structure can be produced with sol-gel method. A significant level has reached by manufacturing technology of optical fiber which utilizes sol-gel method[33], stack and draw method[34], 3D printing method[35] and other technologies.

2.1   Types of PCF

There are two types of PCF,

Hollow-Core PCF

Hollow Core PCF (HC-PCF)[36] is a remarkable innovation in the field of optical fiber technology. Unlike traditional solid-core fibers, HC-PCF features a unique structure with a hollow core surrounded by an intricate arrangement of air holes or periodic dielectric structures that form a photonic crystal lattice. This hollow core design allows for the propagation of light within an air or low-index material-filled core, offering several distinctive advantages. HC-PCF enables a high degree of light confinement in the hollow core, allowing for efficient guidance of light even in unconventional wavelengths, such as the mid-infrared and ultraviolet ranges. This property makes HC-PCF highly suitable for applications ranging from high-power laser delivery and gas sensing to nonlinear optics and ultrafast pulse propagation. The design flexibility of HC-PCF also allows for tailoring its dispersion, nonlinear properties, and other characteristics, opening up new avenues for customization and optimization in various optical applications.
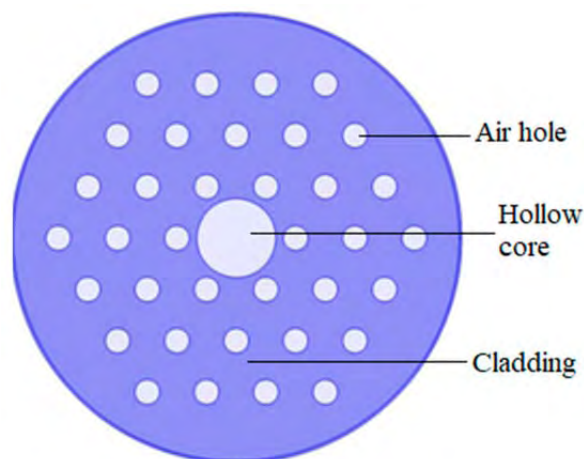

Figure 2.1: Hollow core PCF[37]

Solid-Core PCF

Solid Core Photonic Crystal Fiber[38] (Solid Core PCF) stands as a fundamental advancement in the realm of optical fiber technology. Unlike traditional optical fibers with a continuous solid core, Solid Core PCF is characterized by an intricately designed structure that incorporates an array of air holes or periodic dielectric patterns surrounding a solid core region. This unique configuration brings about remarkable properties that diverge from those of conventional fibers. Solid Core PCF exhibits enhanced light confinement within its solid core, enabling efficient transmission of light across a spectrum of wavelengths. This attribute proves

particularly valuable for applications in nonlinear optics, high-power laser delivery, and specialty fiber optics. By meticulously adjusting the arrangement of air holes or dielectric materials, Solid Core PCF can be tailored to achieve specific dispersion characteristics, nonlinear effects, and other optical attributes. This versatility paves the way for groundbreaking solutions in fields ranging from telecommunications to medical devices, offering unprecedented control over light propagation and interaction within the fiber structure.
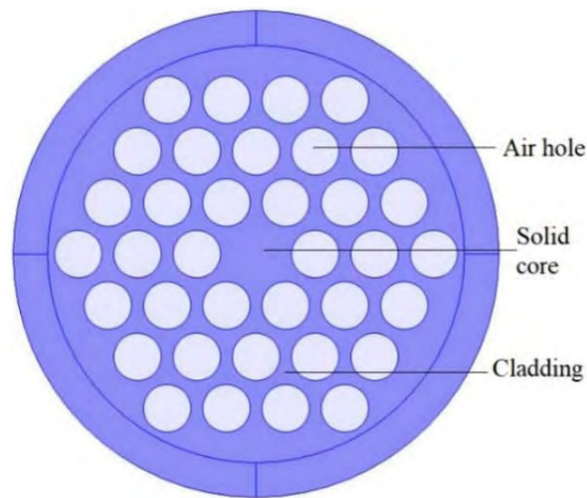

Figure 2.2: Solid core PCF[37]

2.2 Light Guiding Mechanism

There are two main light guiding mechanisms in PCFs[39],

Index Guiding

Index-guiding is the most common light guiding mechanism in PCFs. It works by using the fact that light is bound to propagate in the core of PCF by total internal reflection. The PCF core is made of a higher RI material compared to cladding. The cladding's effective RI(eff-RI) decreases than the core because of air holes and the light confines in the core. This means that light rays that enter the core will be reflected back into the core at the interface of cladding and core. The amount of reflected light is calculated by the variation of RI between the cladding and core. The higher the variation in RI, the lighter will be reflected.

Bandgap Guiding

Bandgap-guiding is a light guiding mechanism that is based on the PBG effect. The photonic bandgap effect occurs when the RI of the material changes periodically in space. This creates a range of frequencies, called the photonic bandgap, for which light cannot propagate in the material. In PCFs, the periodic variation in RI is made with the placement of holes. The RI of holes is less than glass of the core, so they create a photonic bandgap in the cladding. Light that is in the PBG cannot propagate in the cladding, so it is restricted to the core of PCF. By engineering the periodicity and geometry of the microstructures, the bandgap properties can be tailored to match the desired spectral characteristics. This enables PCF to selectively guide light within certain wavelength ranges while prohibiting propagation in others. Bandgap-guiding offers a unique degree of control over light propagation and interaction, making it suitable for various applications. Its adaptability and versatility have led to innovative solutions in optical communications, spectroscopy, and laser science, showcasing the tremendous potential of PCF in advancing photonics technology.

Optical fiber, the traditional medium for transmitting data and information using light, consists of a core surrounded by a cladding layer, enabling the propagation of light through multiple internal reflections. In contrast, photonic crystal fiber introduces a novel design by incorporating an arrangement of microscopic holes that run along the fiber. This unique structure allows for greater control over the guidance and manipulation of light, leading to properties like photonic bandgap effects and high nonlinearity. While conventional optical fibers primarily rely on TIR to guide light, photonic crystal fibers harness intricate light-matter interactions within the periodic arrangement of air holes, permitting tailored dispersion, confinement, and nonlinear responses. This results in opportunities for enhanced light guidance, novel optical effects, and improved transmission properties, making photonic crystal fiber a promising avenue for various applications, including supercontinuum generation, nonlinear optics, and sensing, setting it apart from its conventional optical fiber counterpart.

Chapter 3

Design and Parameter Optimization

Light propagation is significantly influenced by the PCF's design parameters. The hole diameter, pitch distance and the air holes ring number are optimized to get the desired results. Confinement loss, amplitude sensitivity, wavelength sensitivity, sensor length, resolution and figure of merit are the parameters to analyze the performance of the SPR-PCF.

3.1   Geometry of Proposed Sensor

The optical properties of the proposed sensor are modeled and evaluated using COMSOL Multiphysics, as sketched in figure 3.1(a). Figure 3.1(b) shows the enlarged cross-section and dimensions of the sensing channel. The proposed PCF sensor design features a two-ring circular lattice PCF with a small central hole. To absorb radiation, a perfectly matched layer (PML) boundary condition is implemented[40]. The construction of the circular lattice involves a 60-degree anticlockwise rotation of an air hole to form the first ring at a pitch distance. To make the second ring, a 30 degree anticlockwise rotation is done at a double pitch distance from central air hole. Two air holes (i.e one from first ring and the other from second ring) from both sides of the middle hole are removed. The cladding air holes diameter constituting the rings is $1\,\mu$m. The central air hole diameter is $0.3\,\mu$m. The pitch distance is $2\,\mu$m. The thickness of plasmonic material deposited sensing channel is 30nm. In this study, two sensing channels(C-1 and C-2) are proposed and two different regimes are discussed,i.e S-1 and S-2. In S-1, the analytes filled have different refractive indices(nr and nl) and the sensor is operated

9

in visible band. The analyte filled for C-1 is taken nl and the analyte filled for C-2 is taken nr. While in S-2, same analyte refractive index is filled for both the channels(nr=nl=na) and the sensor is operated in n-IR band. The PML is 10 percent of the proposed geometry thickness.
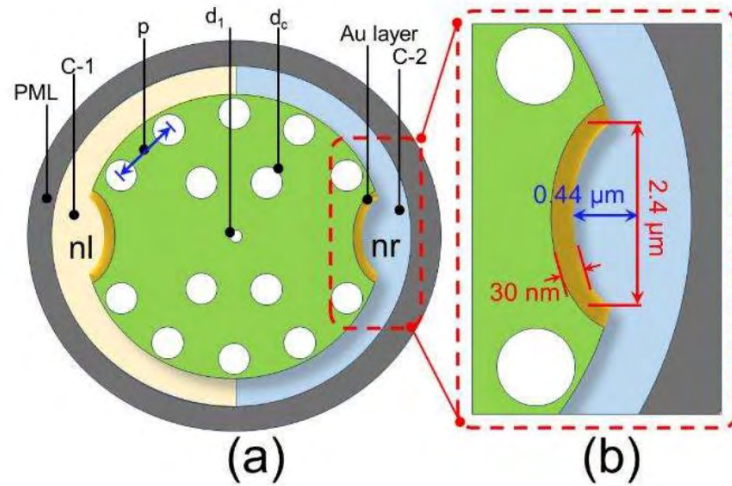

Figure 3.1: Schematic of the suggested PCF geometry

Fused silica and gold are utilized as materials in proposed geometry. The background material used is fused silica for proposed sensor. Sellmeier equation is used to characterize the wavelength-dependent refractive index of silica[41]. The wavelength-dependent dielectric coefficients of gold are characterized by using Drude model[26].

For the realization of the sensor detection system, a standard experimental setup is delineated. The process begins with an optical tunable laser source generating incident light, which is then transmitted through a polarizer controlled by a polarizer-controller. Subsequently, a single-mode fiber (SMF) is employed to introduce linearly polarized light into the suggested plasmonic sensor, with coupling achieved through a splicing technique. To facilitate the introduction and removal of a liquid analyte, an external channel is strategically positioned for analyte flow, and a pump is utilized to regulate the analyte intake and output. The interaction between the analyte and ligand is anticipated to alter the eff-RI of plasmonic mode, creating a shift in resonance wavelength of a signal. The sensor is attached to an optical spectrum analyzer (OSA) through another single-mode fiber, enabling the measurement of transmitted light using the OSA. Subsequently, a computer is employed for the observation and analysis of wavelength peak shifts through the output spectrum. Notably, a shift towards shorter wavelengths is known as a blue
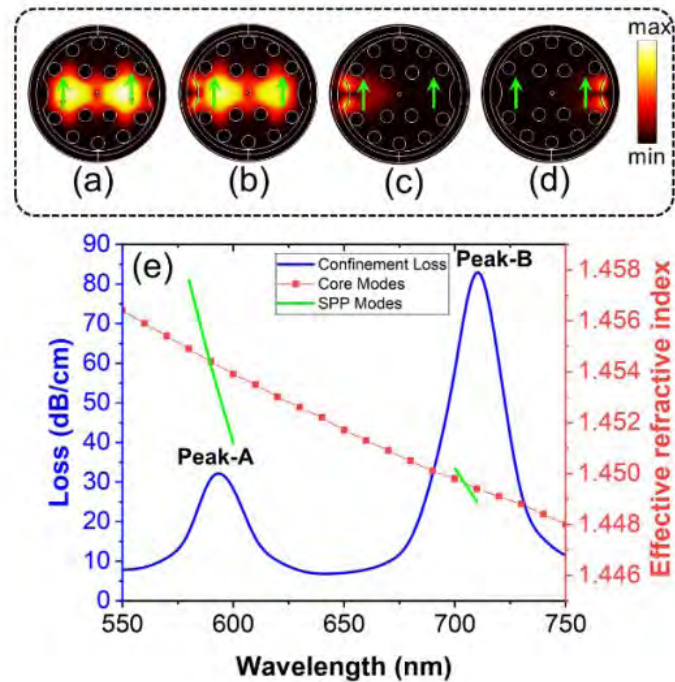
Figure 3.2: provides an illustration of the electromagnetic field distribution and phase-matching within visible band spectroscopy (a) C-2 phase-matching mode, (b) C-1 phase-matching mode, (c) C-1 SPP mode, (d) C-2 SPP mode, and (e) illustrates the interferogram obtained when C-2 (Peak-A) and C-1 (Peak-B) are filled with analytes possessing refractive index nr=1.39 and nl=1.43.
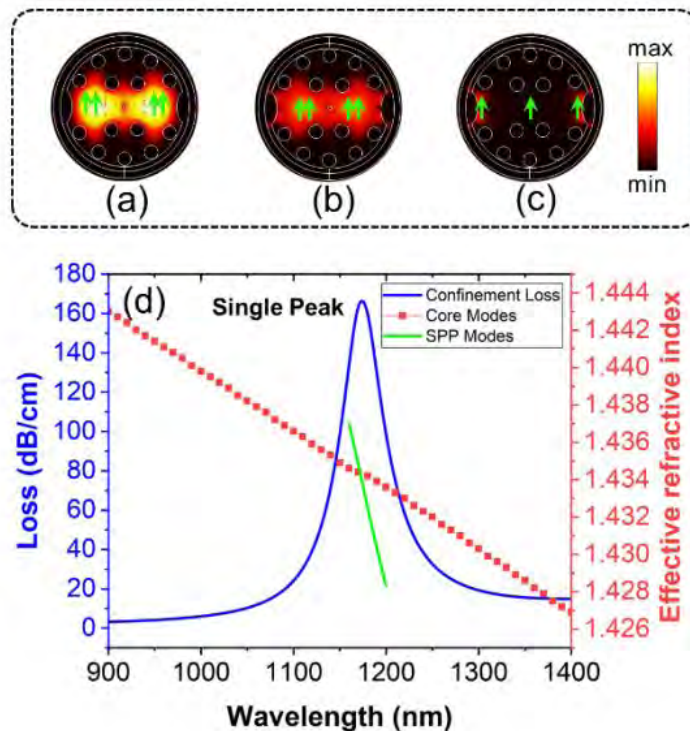

Figure 3.3: provides an illustration of the electromagnetic field distribution and phase-matching within n-IR band spectroscopy (a) core mode, (b) phase-matching mode, (c) C-1 C-2 SPP mode and (d) illustrates the interferogram obtained when C-1 C-2 (produced single peak) are filled with analytes possessing refractive index na=1.25.

shift, while a shift towards longer wavelengths is called a red shift[20].

When the detection channel exhibits no intensity, and energy propagates within the core of the PCF, it is referred to as the core mode, as depicted in figure 3.3(a). Conversely, when the intensity of light is minimal in the core, and vibrant energy resides in the detection channel, it is referred as the Surface Plasmon Polariton (SPP) mode, as depicted in figure 3.2(c) and (d). In case of coupled mode, both the fiber core and sensing channel possess energy[42], as shown in figure 3.2(c). At phase-matching, the sensor demonstrates maximum confinement loss. Phase-matching occurs when the real component of eff-RI for core mode equals the real component of the effective RI for SPP mode. The eff-RI varies with the operating wavelength. Phase-matching happens when the photons frequency matches the frequency of free electrons at metal surface, resulting in resonance wavelength. Consequently, a significant portion of energy transitions from the core to the SPP mode. Y-polarized modes are analyzed to assess the sensor's response because the imaginary part of the eff-RI for y-polarized modes is greater than that of x-polarized modes due to lower plasmon damping in the x-polarization. In figure 3.2(e) and figure 3.3(d), the blue lines illustrate the variation of confinement loss corresponding to wavelength shifts. The red line with symbols signifies the eff-RI of core mode, while the green line represents the eff-RI of the SPP mode. The resonance wavelength is a point where red and green lines intersect, satisfying the coupled mode condition for a loss peak. Confinement loss is maximal at the resonance wavelength, indicating the highest energy transfer. For S-1, the eff-RI of core mode and SPP mode aligns at the operating wavelength of 594 nm (peak-A), with a loss peak of 33.598 dB/cm for an analyte RI of 1.39 filled at C-2 and the phase-matching occurs at wavelength of 712.5 nm (peak-B) for analyte refractive index of 1.43 filled at C-1 having loss peak of 88.006 dB/cm, as depicted in figure 3.2. While for S-2, the resonance wavelength is 1173.9 nm (single peak), with a confinement loss 166.75 dB/cm when both channels are filled with analyte refractive index of 1.25, as shown in figure 3.3.

3.2   Analysis Parameters

The parameters to evaluate the performance of SPR based PCF are discussed below.

Confinement Loss

The basic parameter to evaluate the performance of sensor is confinement loss(CL). Confinement loss is controlled with optimizing structural parameters of PCF. CL is evaluated by equation[43],

$$\alpha = 8.686 \cdot \frac{2\pi}{\lambda} \cdot \text{Im}(n_{\text{eff}}) \ (\text{dB/cm}) \tag{3.1}$$

Where α is the CL, λ is operating wavelength, and imaginary component of effective RI is denoted as Im(neff). Confinement loss is maximum for the wavelength of phase-matching condition.

Interrogation Methods

Sensitivity tells us that how much the output of sensor varies with the variation of refractive index. The two sensitivity interrogation methods are used for SPR based PCF. One is called wavelength sensitivity and the other is called amplitude interrogation method.

Wavelength Sensitivity

Wavelength Sensitivity(WS) tells us about the change of resonance wavelength because of the change in RI of analyte and it is evaluated by[44],

$$WS = \frac{\Delta\lambda_{\text{peak}}}{\Delta n_a} \ \left(\frac{\text{nm}}{\text{RIU}}\right) \tag{3.2}$$

Δn_a denotes the variation in analyte RI and $\Delta\lambda_{\text{peak}}$ is shift of resonance wavelength.

Amplitude Sensitivity

The performance of a suggested sensor can also be evaluated by amplitude sensitivity(AS). The amplitude sensitivity refers to how much the amplitude of the transmitted light changes in response to variations in the external parameter. Amplitude Sensitivity is evaluated by[45],

$$AS = -\frac{1}{\alpha(\lambda, n_a)}\frac{\partial\alpha(\lambda, n_a)}{\partial n_a} \ \left(\text{RIU}^{-1}\right) \tag{3.3}$$

$\alpha(\lambda, n_a)$ is CL at a specific analyte RI and particular wavelength. $\partial\alpha(\lambda, n_a)$ is difference of two CL curves due to any variation of analyte RI, and ∂n_a represents

the change of analyte RI. Amplitude sensitivity is economic and simple because wavelength interpolation is not needed for it.

Sensor Length

Sensor length(L) is the reciproacal of the confinement loss for the particular analyte at resonance wavelength. The sensor length decreases with the rise of CL[29].

$$L = \frac{1}{\alpha(\lambda, n_a)} \tag{3.4}$$

$\alpha(\lambda, n_a)$ is CL at a specific RI of analyte and particular wavelength. The decrease of sensor length with the rise of analyte RI assures that the suggested sensor is a miniaturized probe[46]. Excessive loss would impede the input light from reaching the output port. Conversely, an extremely low loss value would result in very weak coupling. Therefore, achieving an optimal value is crucial for an effective sensor[25].

Resolution

The resolution is another crucial factor to determine the smallest variation of analyte RI. It is linked to accuracy of sensor. Resolution tells how small a variation of analyte RI can be determined. Resolution is evaluated by,

$$R = \frac{\Delta\lambda_{\min}}{WS} \text{ (RIU)} \tag{3.5}$$

Where $\Delta\lambda_{\min}$ represents minimum shift of wavelength, which is considered 0.1nm for the calculations of suggested sensor and WS is the wavelength sensitivity for analyte. If the resonance wavelength shift is longer, then the sensor resolution will be lower. Therefore, such sensor can precisely sense the small variation in refractive index of analyte. Instrumental noise and additional noise due to external perturbations can be ignored while calculating the sensor resolution[20].

Figure of Merit

The ratio of sensitivity to full width half maximum(FWHM) is called figure of merit(FOM). FOM is evaluated by using the formula[47],

$$FOM = \frac{WS}{FWHM} \ (RIU^{-1}) \tag{3.6}$$

3.3 Gold Thickness Optimization

The thickness of gold(Au) layer can be changed to alter the sensor's performance. Rise in number of carriers of metal due to increase in gold layer thickness give rise to a greater number of electrons participating in surface plasmon resonance, resulting in increase of energy and phase-matching condition occurs at shorter wavelength showing blue-shift. On the other hand, phase delay effect happens when the Au layer thickness is more than penetration depth of electric field. The loss peak and resonance intensity decreases with the dominant role of phase delay effect. When the increase in free charges play a major role, the loss peak and resonance intensity increases. The maximum loss and resonance intensity remain unaffected when increasing electron number and phase delay effect are equalized. Thus, the sensor performance could be adjusted accordingly by varying the thickness of gold layer[32].
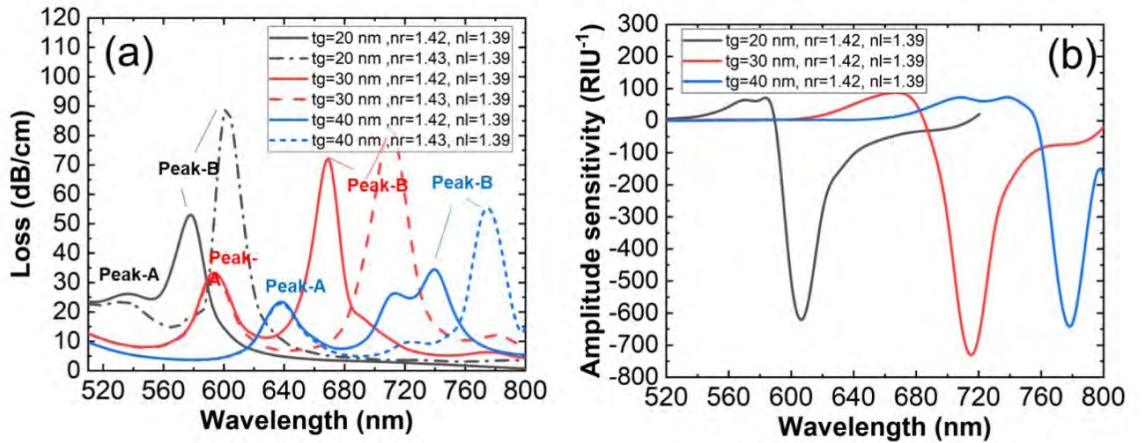

Figure 3.4: (a) illustrates the variation of confinement loss for Peak-A and Peak-B corresponding Au thickness changed from 20 nm to 40 nm; and (b) depicts corresponding amplitude sensitivity.

The Au layer thickness is taken 20 nm, 30 nm and 40 nm for RI of 1.39 for C-1 and 1.43 for C-2 using visible band, as shown in figure 3.4. The loss peak (peak-B) for 1.43 is greatest with 20 nm thickness of gold but the loss peak (peak-A) of 1.39 is not sharp and the difference between the resonance wavelengths for the two peaks is also less. The loss peak value of 1.39 is 33.598 dB/cm for 30 nm thickness and 23.633 dB/cm for 40 nm thickness of gold. The peak CL for 1.43 is 86.49 dB/cm with 30 nm thickness and 62.073 dB/cm for 40 nm thickness of

gold while the loss for 1.42 RI of C-2 is 71.38 dB/cm for 30 nm and 34.414 dB/cm for 40 nm but the appearance of third peak is contradictory, as shown in figure 3.4(a). The maximum amplitude sensitivity values for 20 nm, 30 nm and 40 nm are -585.019 RIU^{-1}, -674.087 RIU^{-1} and -632.048 RIU^{-1}, as depicted in figure 3.4(b). Based on resultant profile of confinement loss for Peak-A and Peak-B and obtained amplitude sensitivities, it has been determined that the optimum Au thickness for the suggested sensor is 30 nm.

Chapter 4

Results and Discussion

The results are evaluated by using finite element method in COMSOL Multiphysics. The Finite Element Method is a numerical method to solve boundary value problems using partial differential equations (PDEs) by dividing a complex domain into smaller, simpler subdomains (finite elements) and approximating the behavior of the solution within each element. The method involves discretizing the domain, applying appropriate approximations to the governing equations, and then solving the resulting system of algebraic equations. FEM is used in many fields, including fluid dynamics, structural analysis, electromagnetics, and heat transfer to simulate and analyze complex physical phenomena. In the context of PCF, FEM can be employed to model the light propagation within the fiber, considering the intricate geometries and material properties involved. This allows researchers and engineers to study the behavior of light in photonic crystal fibers and design novel optical devices with specific properties. Mode analysis is used for numerical investigation of proposed sensor with optimized parameters.

4.1 Analysis of S-1

In S-1, the analytes filled for both the channels have different refractive index. To check the performance, sensor is operated in the visible band.
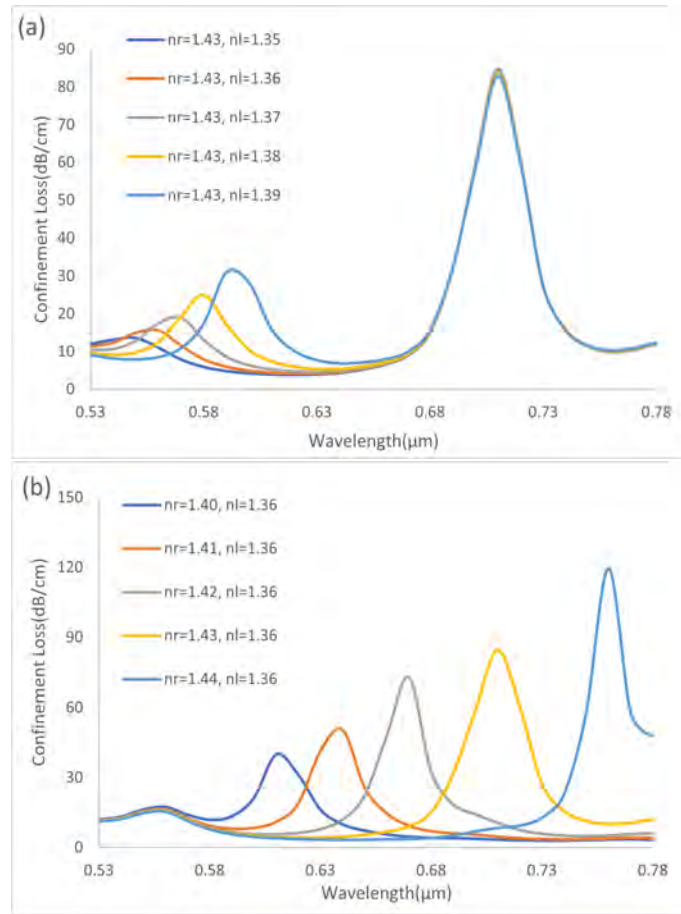
Figure 4.1: Confinement loss by varying analyte RI to characterize the peak shifts from (a) 1.35 to 1.39 for C-1, (b) 1.40 to 1.44 for C-2

The graphs in figure 4.1 represents the change of confinement loss with wavelength for S-1. The refractive index is varied with the step size of 0.01. In this scenario, nr is kept constant at 1.43 and nl is varied from 1.35 to 1.39, as shown in figure 4.1(a). The confinement loss for 1.35, 1.36, 1.37, 1.38 and 1.39 is 13.824 dB/cm, 16.028 dB/cm, 19.568 dB/cm, 25.103 dB/cm, and 33.598 dB/cm at operating wavelength 0.5473 µm, 0.5565 µm, 0.5669 µm, 0.5791 µm,0.594 µm,respectively, keeping nr same. Then, the RI of C-2 is varied from 1.40 to 1.44 and nl is kept constant at 1.36. The confinement loss for 1.40, 1.41, 1.42, 1.43 and 1.44 is 41.818 dB/cm, 57.249 dB/cm, 79.849 dB/cm, 88.006 dB/cm, and 144.3 dB/cm at operating wavelength 0.6126 µm, 0.6361 µm, 0.6673 µm, 0.7125 µm,0.7573 µm,respectively, having nl=1.36, as shown in figure 4.1(b).
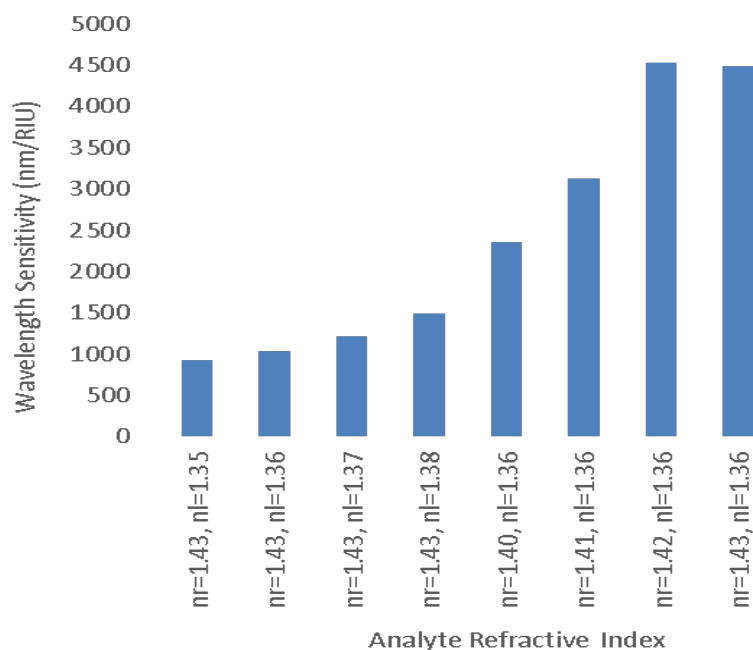
Figure 4.2: Bar graph showcase the incremental trend of wavelength sensitivity produced by the PCF sensor employing Peak-A and Peak-B in the visible band.

The graph in figure 4.2 depicts the change of wavelength sensitivity with the analyte RI change in visible band. For C-1, the wavelength sensitivity varies from 920 nm/RIU to 1490 nm/RIU.The max-WS is 1490 nm/RIU at nl=1.39 and nr=1.43. The wavelength sensitivity values are 920 nm/RIU, 1040 nm/RIU and 1220 nm/RIU for nl of 1.35, 1.36 and 1.37, respectively, keeping nr constant at 1.43. For C-2, the wavelength sensitivity varies between 2350 nm/RIU and 4520 nm/RIU. The max-WS is 4520 nm/RIU at nr=1.42 with nl at 1.36. The wavelength sensitivity values are 2350 nm/RIU, 3120 nm/RIU and 4480 nm/RIU for nr of 1.40, 1.41 and 1.43, respectively, for same nl of 1.36. The wavelength sensitivity demonstrates a continuous trend with the change in the RI of the analyte.
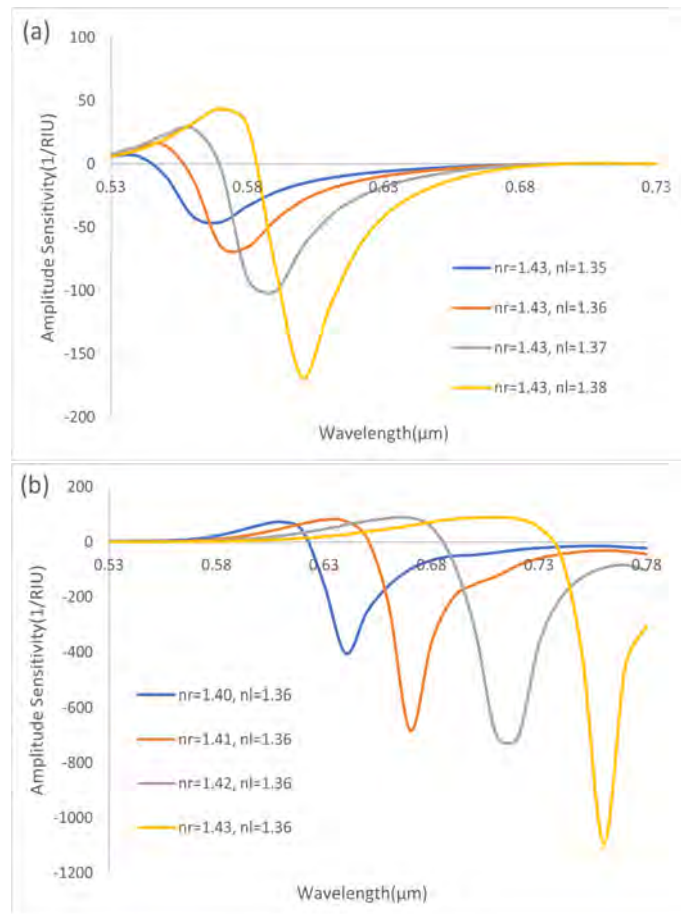
Figure 4.3: Amplitude sensitivity of the suggested PCF sensor for S-1: (a) C-1 with analyte RI varying from 1.35 to 1.38 and (b) C-2 with analyte RI varying from 1.40 to 1.43.

Figure 4.2 illustrates the amplitude sensitivity response for various refractive indices of analyte using visible band. In S-1, the max-AS is -168.13 RIU^{-1} at nl=1.39 and amplitude sensitivity is -45.87 RIU^{-1} at nl=1.35 when nl is varied from 1.35 to 1.39 having nr constant at 1.43. The amplitude sensitivity values are -65.59 RIU^{-1} and -100.7 RIU^{-1} with the RI of 1.36 and 1.37, respectively for C-1, as depicted in figure 4.2(a). For C-2, the amplitude sensitvity is -405.09 RIU^{-1} for nr at 1.40 having nl at 1.36 and the max-AS is -1093.29 RIU^{-1} for nr at 1.43 keeping nl at 1.36. The amplitude sensitivity values are -682.1 RIU^{-1} and -708.57 RIU^{-1} with the RI of 1.41 and 1.42, respectively for C-2, as depicted in figure 4.2(b).
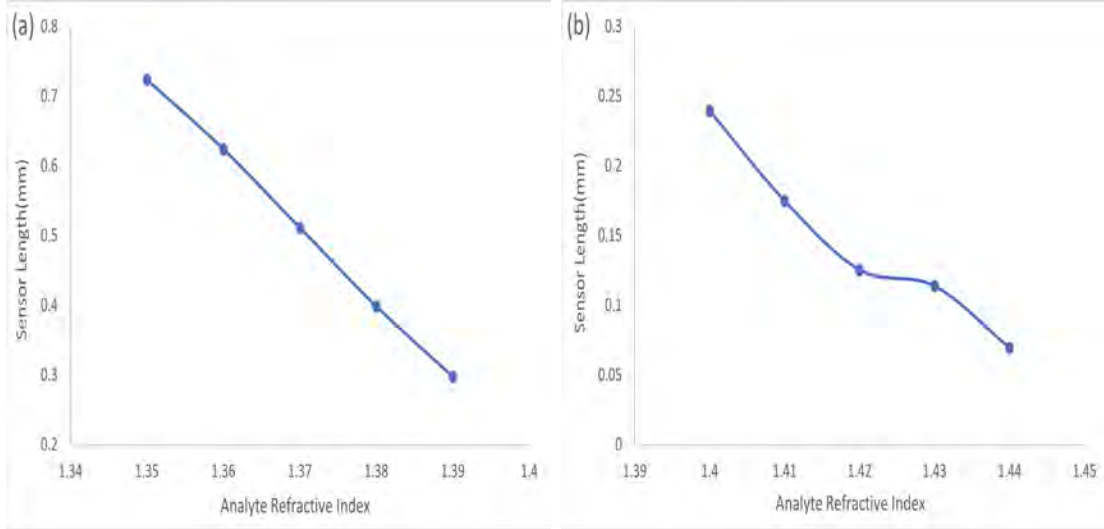
Figure 4.4: Sensing length as function of analytes RIs for S-1: (a) C-1 with analyte RI varying from 1.35 to 1.39 and (b) C-2 with analyte RI varying from 1.40 to 1.43.

The sensor length varies between 0.723 mm at nr=1.43,nl=1.35 to 0.297 mm at nr=1.43,nl=1.39 for C-1 as shown in figure 4.4(a). Similarly, the sensor length varies between 0.239 mm at nr=1.41,nl=1.36 to 0.069 mm at nr=1.44,nl=1.36 for C-2 as shown in figure 4.4(b). Such decreasing trend of sensor length with rise of refractive index assures that the proposed sensor is a miniaturized probe.

The maximum FOM reported for proposed sensor is 230.56 RIU^{-1} having FWHM of 19.6 nm, when the analyte RI for C-1 is 1.36 and C-2 is 1.42. For C-1, the resolution varies from 1.08×10^{-4} for nl=1.35 to 6.71×10^{-5} for nl=1.38 when refractive index for C-2 is kept constant at 1.43. The resolution values for nl of 1.36 and 1.37 are 9.61×10^{-5} and 8.19×10^{-5}, respectively, keeping refractive index constant for C-2 at 1.43, as presented in Table 4.1. For C-2, the finest wavelength resolution is 2.23×10^{-5} for nr=1.43, nl=1.36. The resolution values for nl of 1.40, 1.41, and 1.42 are 4.25×10^{-5}, 3.2×10^{-5} and 2.21×10^{-5}, respectively, keeping refractive index constant for C-1 at 1.36, as presented in Table 4.2.

The comprehensive performance summary of the proposed sensor, highlighting key factors including resonance wavelength (λ), wavelength shift ($\Delta\lambda$), confinement loss (CL), sensing length (L), wavelength sensitivity (WS), amplitude sensitivity (AS), and sensor resolution (R), is presented in Table 4.1 for visible band investigations.

Table 4.1: Performance of the S-1 with varied nl

nr	nl	λ (μm)	$\Delta\lambda$ (nm)	CL (dB/cm)	L (mm)	WS (nm/RIU)	AS (RIU^{-1})	Resolution (RIU)
1.43	1.35	0.5473	9.2	13.824	0.723	920	-45.87	1.08×10^{-4}
1.43	1.36	0.5565	10.4	16.028	0.623	1040	-65.59	9.61×10^{-5}
1.43	1.37	0.5669	12.2	19.568	0.511	1220	-100.7	8.19×10^{-5}
1.43	1.38	0.5791	14.9	25.103	0.398	1490	-168.13	6.71×10^{-5}
1.43	1.39	0.594		33.598	0.297			

Table 4.2: Performance of the S-1 with varied nr

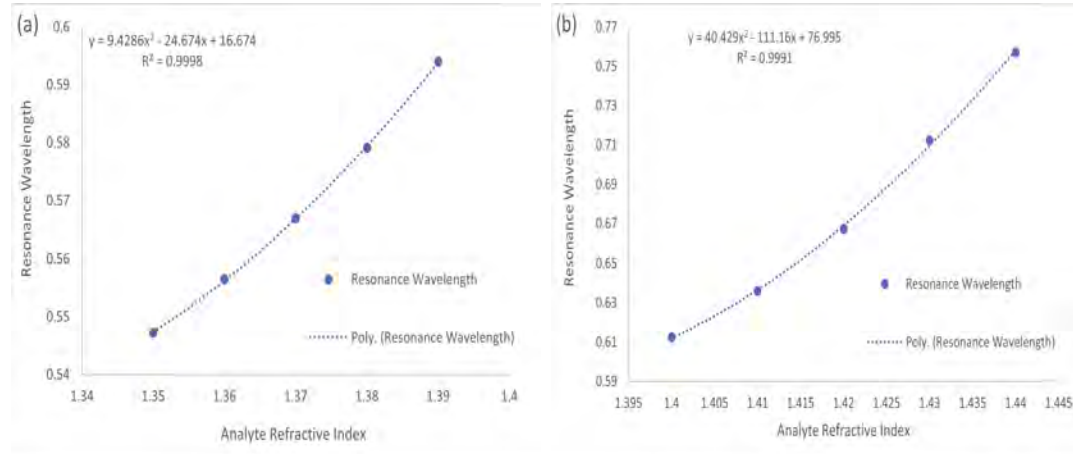| nr	nl	λ (μm)	$\Delta\lambda$ (nm)	CL (dB/cm)	L (mm)	WS (nm/RIU)	AS (RIU^{-1})	Resolution (RIU)
1.4	1.36	0.6126	23.5	41.818	0.239	2350	-405.09	4.25×10^{-5}
1.41	1.36	0.6361	31.2	57.249	0.174	3120	-682.1	3.2×10^{-5}
1.42	1.36	0.6673	45.2	79.849	0.125	4520	-708.57	2.21×10^{-5}
1.43	1.36	0.7125	44.8	88.006	0.113	4480	-1093.29	2.23×10^{-5}
1.44	1.36	0.7573		144.3	0.069			

Figure 4.5: Illustrates the polynomial fitting of the PCF sensor using (a) C-1 and (b) C-2 in S-1

The polynomial fitting of analyte RI versus resonance wavelength significantly influences resolution and average sensitivity. The curve fitting depicting the change of resonance wavelength with the analyte RI for C-1 and C-2 with S-1 are shown in figures 4.5(a,b), respectively. The R^2 of the curve fitting are 0.9998 and 0.9991 while the corresponding equations are $y = 9.4286x^2 - 24.674x + 16.674$ and $y = 40.429x^2 - 111.16x + 79.995$ for C-1 and C2 of S-1, respectively, which makes the proposed sensor feasible for practical uses. In case of PCF sensor, the wavelength sensitivity rises with the rise of refractive index because the loss peak

moves to higher wavelength when the analyte refractive index increases.

4.2   Analysis of S-2

In S-2, the suggested sensor is operated in n-IR band with same analyte refractive index filled at C-1 and C-2.
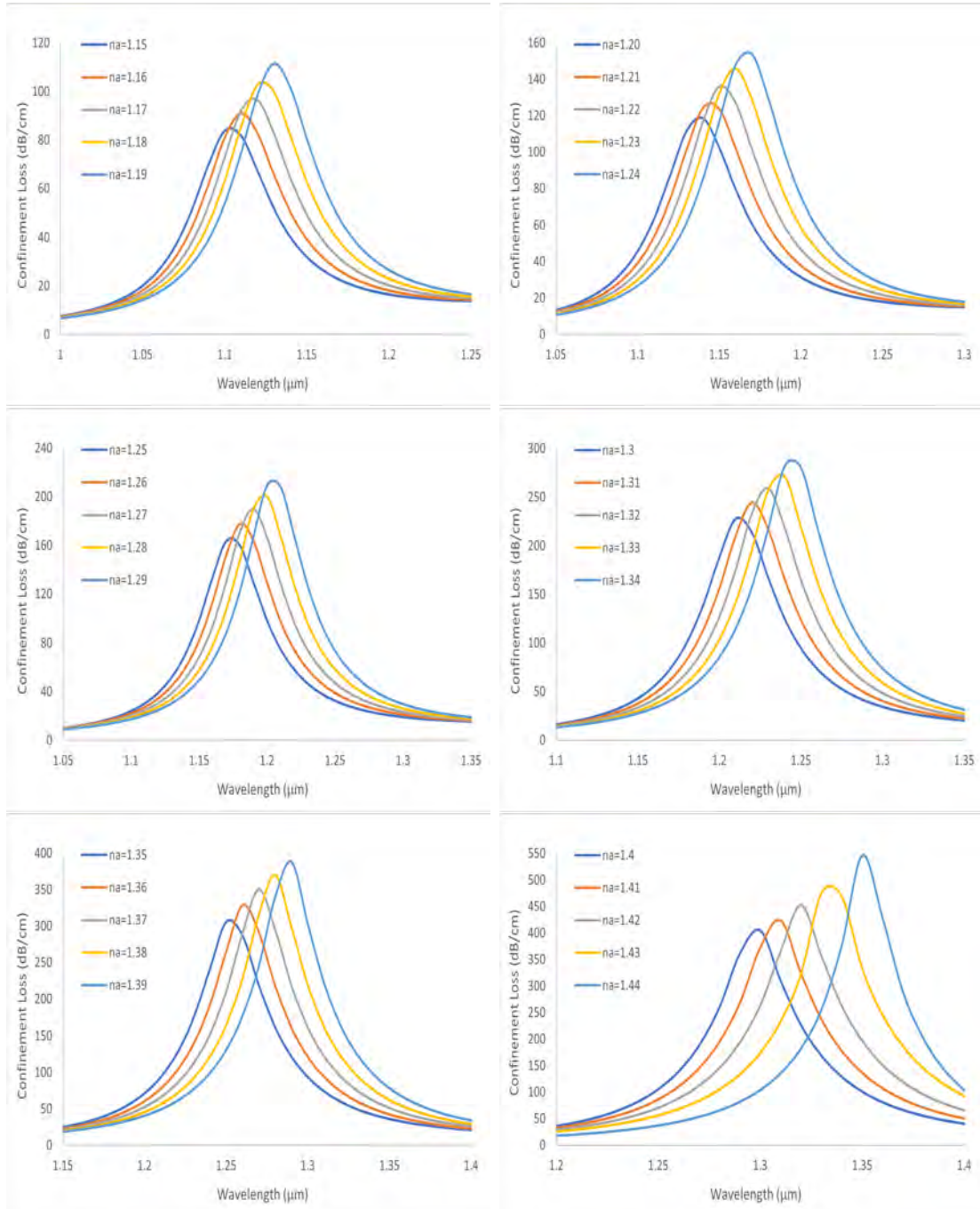

Figure 4.6: Confinement loss by varying analyte RI to characterize the peak shifts when both C-1 and C-2 are varied from 1.15 to 1.44.

For S-2, a minimum loss for single peak occurs at RI na=1.15 with optimized

parameters is 85.175 dB/cm at resonant wavelength of 1.0853 µm while the maximum loss peak is observed for RI na=1.44 with optimized parameters is 582.53 dB/cm at wavelength of 1.3529 µm, as shown in figure 4.6. The value of CL peak increases with the rise of analyte RI. It can also be observed from all graphs that the rise in analyte RI shows red shift for phase-matching conditions. The peak values of CL vary at different wavelengths for all RIs. The difference between the core and surface plasmon polariton (SPP) mode reduces with the increase in analyte RI, leading to the rise of the loss peak value.
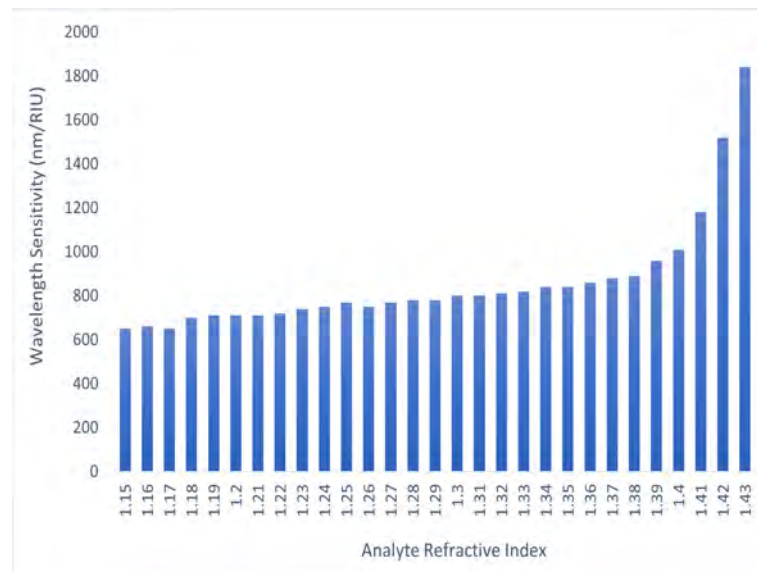
Figure 4.7: Bar graph showcases the incremental trend of wavelength sensitivity produced by the PCF sensor in the n-IR band.

Figure 4.7 illustrates the wavelength sensitivity trend for S-2. The maximum wavelength sensitivity occurs for a shift in the analyte RI from 1.43 to 1.44, reporting a value of 1840 nm/RIU which is relatively low. It is noteworthy that within this range, the sensor covers a wide range of analyte detection from 1.15 to 1.44. This wide detection range is highly desirable for numerous bio and chemical applications.
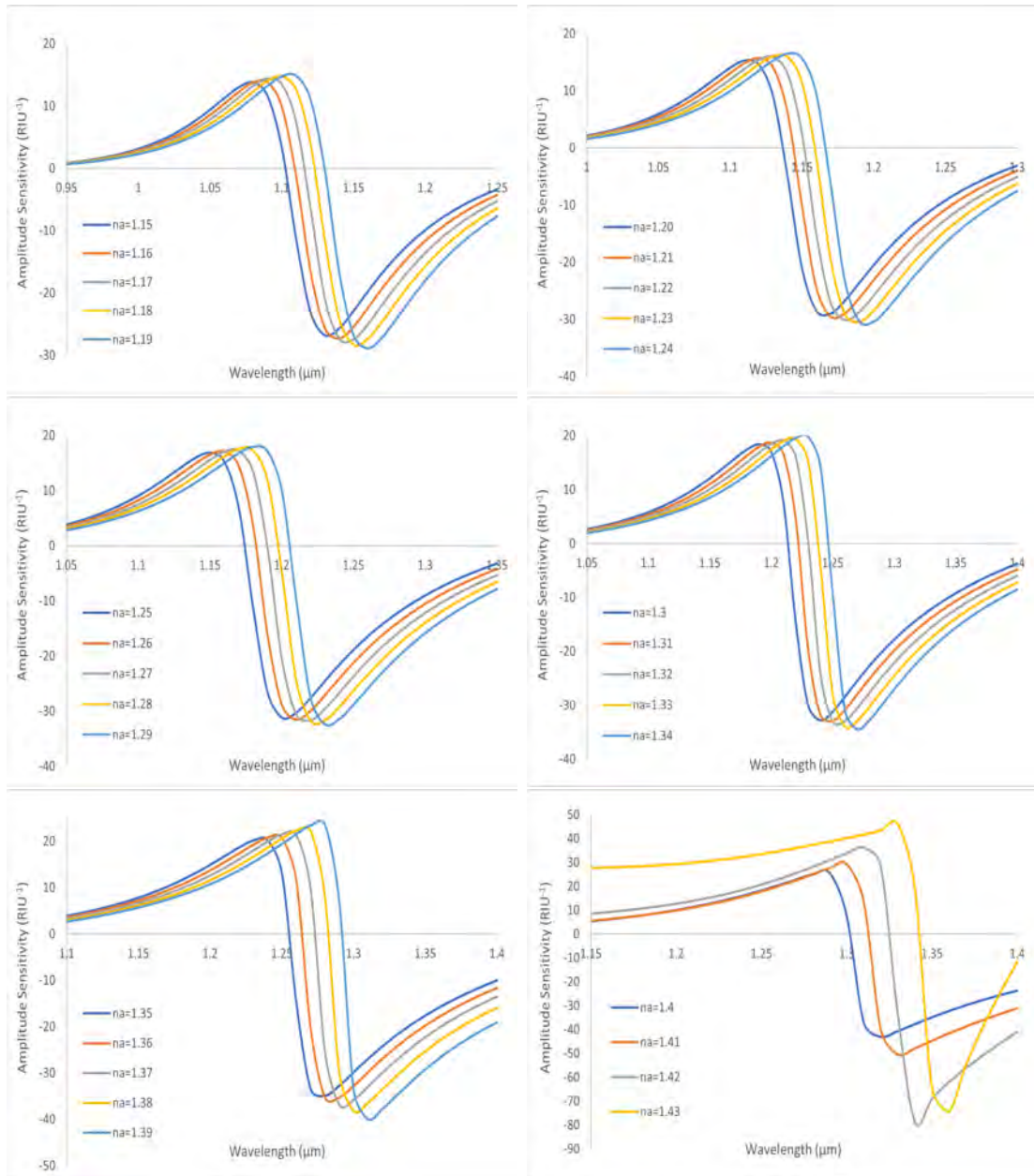
Figure 4.8: Amplitude sensitivity of the suggested PCF sensor for both C-1 and C-2 with varied analyte RIs from 1.15 to 1.43 in the n-IR regime

Using the n-IR band, both C-1 and C-2 are exposed to analyte RIs ranging from 1.15 to 1.44 with a step size of 0.01, as shown in figure 4.8. The amplitude sensitivity value is 26.7465 RIU^{-1} for the analyte RI of 1.15 at an wavelength of 1.13 µm. The max-AS value is 78.7063 RIU^{-1} for the RI of 1.42 at an operating wavelength of 1.34 µm. Although relatively low, this value covers a wider sensing range.
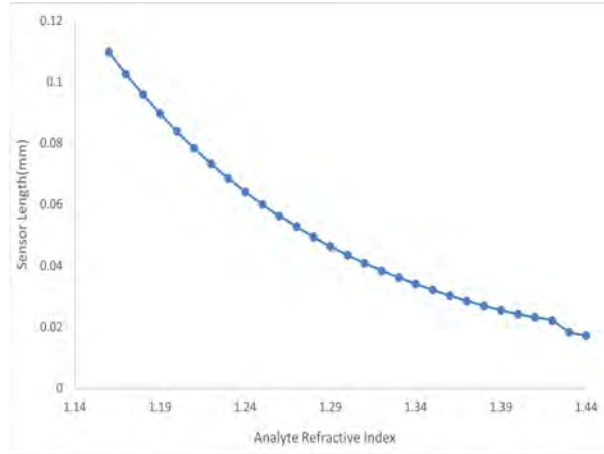
Figure 4.9: Sensing length as function of analytes RIs for S-2.

The sensor length varies between 0.117 mm to 0.01716 mm for S-2, as shown in figure 4.9. The finest wavelength resolution for S-2 is 5.43×10^{-5} at refractive index of 1.43, as presented in Table 4.3. The FWHM for analyte RI of 1.43 comes out to be 41.63 nm for S-2. The WS reported for the RI of analyte 1.43 is 1840 nm/RIU. The FOM is 44.19 RIU^{-1} for the refractive index of 1.43.
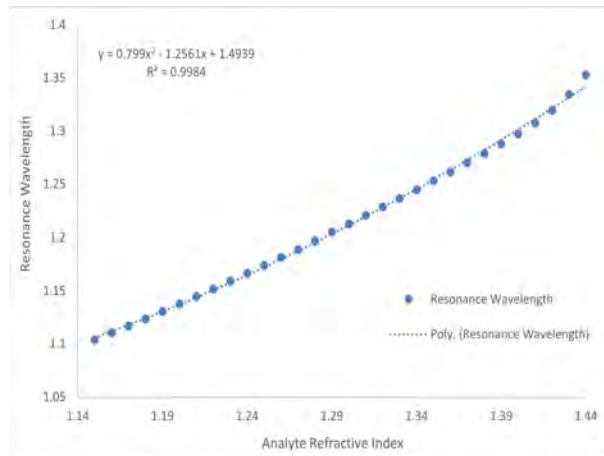
Figure 4.10: Illustrates the polynomial fitting of the PCF sensor using C-1 and C-2 for S-2

The fitting lines for the change of resonance wavelength with the variation of analyte RI for S-2 is shown in figure 4.10. The R^2 value of the curve fitting is 0.9984 with the corresponding equation $y = 0.799x^2 - 1.2561x + 1.4939$ for S-2.

The comprehensive performance summary of the proposed sensor, highlighting key factors including resonance wavelength (λ), wavelength shift ($\Delta\lambda$), confinement loss (CL), sensing length (L), wavelength sensitivity (WS), amplitude sensitivity (AS), and sensor resolution (R), is presented in Table 4.3 for n-IR band investiga-

tions.

Table 4.3: Performance of the sensor in n-IR band spectroscopy

na	λ (μm)	$\Delta\lambda$ (nm)	CL (dB/cm)	L (mm)	WS (nm/RIU)	AS (RIU^{-1})	Resolution (RIU)
1.15	1.1039	6.5	85.175	0.117	650	-26.74	1.54×10^{-4}
1.16	1.1104	6.6	91.082	0.109	660	-27.27	1.52×10^{-4}
1.17	1.117	6.5	97.428	0.102	650	-27.41	1.54×10^{-4}
1.18	1.1235	7	104.23	0.095	700	-28.29	1.43×10^{-4}
1.19	1.1305	7.1	111.53	0.089	710	-28.82	1.41×10^{-4}
1.2	1.1376	7.1	119.33	0.083	710	-29	1.41×10^{-4}
1.21	1.1447	7.1	127.67	0.078	710	-29.51	1.41×10^{-4}
1.22	1.1518	7.2	136.56	0.073	720	-30.13	1.39×10^{-4}
1.23	1.159	7.4	146.02	0.068	740	-30.39	1.35×10^{-4}
1.24	1.1664	7.5	156.08	0.064	750	-30.4	1.33×10^{-4}
1.25	1.1739	7.7	166.75	0.059	770	-31.1	1.30×10^{-4}
1.26	1.1816	7.5	178.05	0.056	750	-31.52	1.33×10^{-4}
1.27	1.1891	7.7	189.98	0.052	770	-31.65	1.30×10^{-4}
1.28	1.1968	7.8	202.58	0.049	780	-31.65	1.28×10^{-4}
1.29	1.2046	7.8	215.85	0.046	780	-32.36	1.28×10^{-4}
1.3	1.2124	8	229.82	0.043	800	-32.75	1.25×10^{-4}
1.31	1.2204	8	244.52	0.040	800	-32.91	1.25×10^{-4}
1.32	1.2284	8.1	259.97	0.038	810	-33.02	1.23×10^{-4}
1.33	1.2365	8.2	276.23	0.036	820	-33.89	1.22×10^{-4}
1.34	1.2447	8.4	293.35	0.034	840	-34.47	1.19×10^{-4}
1.35	1.2531	8.4	311.4	0.032	840	-34.9	1.19×10^{-4}
1.36	1.2615	8.6	330.43	0.030	860	-35.27	1.16×10^{-4}
1.37	1.2701	8.8	350.43	0.028	880	-36.8	1.14×10^{-4}
1.38	1.2789	8.9	371.27	0.026	890	-38.22	1.12×10^{-4}
1.39	1.2878	9.6	392.51	0.025	960	-39.98	1.04×10^{-4}
1.4	1.2974	10.1	413.6	0.024	1010	-43.03	9.90×10^{-5}
1.41	1.3075	11.8	432.25	0.023	1180	-50.44	8.47×10^{-5}
1.42	1.3193	15.2	453.41	0.022	1520	-78.7	6.58×10^{-5}
1.43	1.3345	18.4	544.16	0.018	1840	-74.18	5.43×10^{-5}
1.44	1.3529		582.53	0.017			

A comparison is conducted as shown in Table 4.4, highlighting the distinctive features of the proposed sensor compared to the sensors reported earlier. The sensor stands out in terms of its dual-regime detection (i.e. visible and n-IR), offering a wide range of sensing capabilities and enabling a multi-analyte detection system.

Table 4.4: Comparison of the sensor

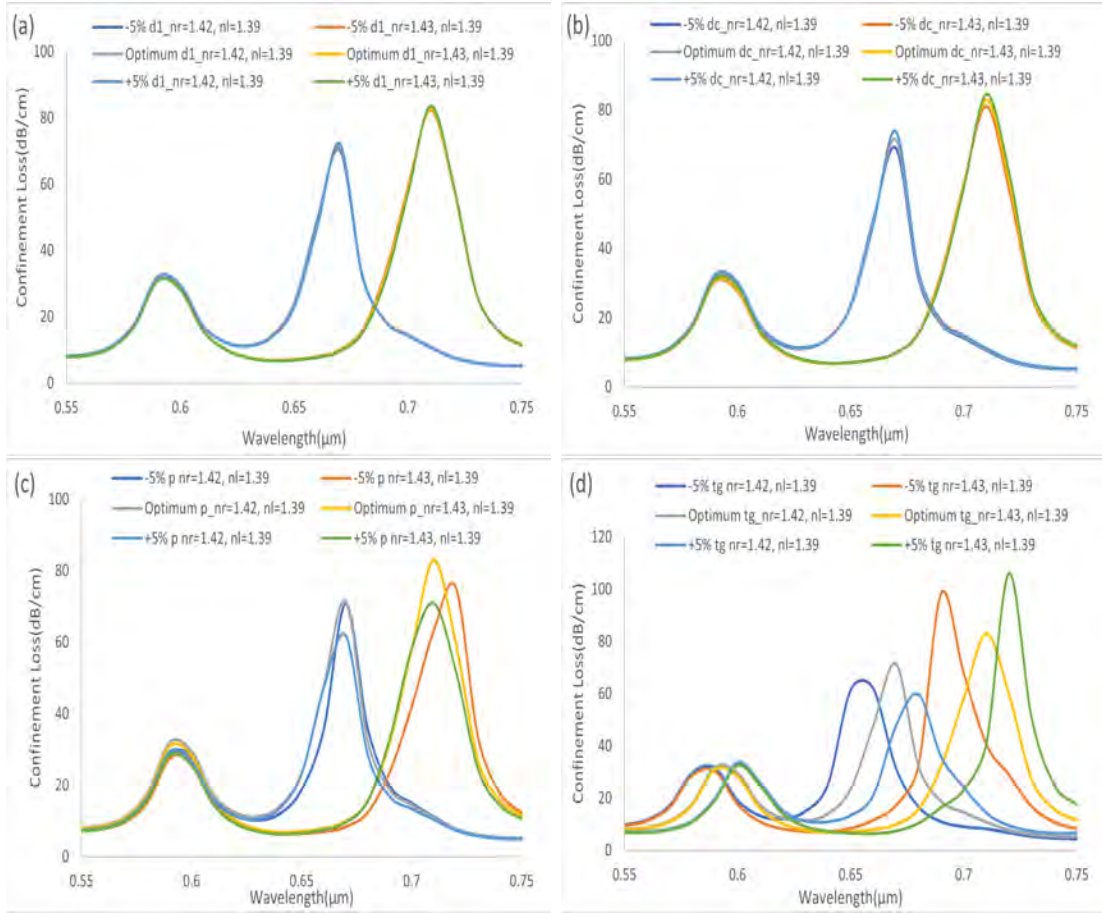| Ref	Sensing Method/ Channels	Plasmonic Material	Sensing Range	**WS** (nm/RIU)	**AS** (RIU^{-1})	**Wavelength** Resolution (RIU)
[22]	External	Gold	1.26-1.38	5626		1.7×10^{-5}
[23]	External	Gold	1.18-1.36	20000	1054	5.0×10^{-6}
[24]	External	Gold	1.13-1.35		17500	5.7×10^{-6}
[25]	External	Gold	1.15-1.36	12600	726	7.9×10^{-6}
[26]	External	Gold	1.20-1.40	5000	1277	2.0×10^{-5}
[28]	External/C-1	Gold	1.33-1.40	12000	807	8.3×10^{-6}
	Internal/C-2		1.33-1.39	10000	569	1.0×10^{-5}
[29]	External/C-1	Gold	1.32-1.35	3000	287	3.3×10^{-5}
	External/C-2		1.36-1.39	25000	928	4.0×10^{-6}
[30]	External/C-1	Gold	1.30-1.34	3392	148	2.9×10^{-5}
	External/C-2		1.35-1.39	6664	217	1.5×10^{-5}
	External/C-3		1.40-1.44	10243	167	9.7×10^{-6}
[48]	External/C-1	Ag with	1.33-1.366	2500		4.0×10^{-5}
	External/C-2	Graphene		3083		3.2×10^{-5}
		Coating				
This	External/C-1	Gold	1.35-1.39	1490	168	6.7×10^{-5}
Work	External/C-2		1.40-1.44	4520	1093	2.2×10^{-5}
	External/C-1,C-2		1.15-1.44	1840	78	5.4×10^{-5}

Figure 4.11: Fabrication tolerance of (a) d1, (b) dc, (c) Pitch distance, and (d) Gold layer thickness

4.3   Fabrication Tolerance

The fabrication of the sensor with exact optimal parameters poses challenges in practical applications. To assess the sensor's feasibility, the parameters are systematically varied by decreasing and increasing 5 percent from the optimum values, and the sensor's response is evaluated. Fabrication tolerance is calculated by setting the analyte RI for C-1 at 1.39, and for C-2, RIs of 1.42 and 1.43 are considered. As C-1 is fixed, therefore, variations in Peak-B are analyzed corresponding to deviations in loss peaks for C-2 while considering a fabrication tolerance of ± 5 percent. From figures 4.11(c-d), it is evident that CL and peak shift exhibit significant variations with changes in pitch and Au thickness. In contrast, no significant variations are observed by varying the diameter of air-holes, as shown in figures 4.11(a-b). Based on these findings, the optimal parameters for the proposed PCF considering the fabrication feasibility are provided in figures 4.11(a-d).

Chapter 5

Conclusion

In conclusion, this study presents a straightforward yet highly effective dual-core PCF sensor exploiting surface plasmon resonance, numerically investigated for both visible and n-IR regimes with multi-analyte sensing capabilities using COMSOL Multiphysics. The sensor's simplicity arises from its exterior sensing channel, with gold employed as the plasmonic material. With dual channels, the proposed sensor demonstrates the ability to simultaneously sense multiple analytes in visible band, while also providing a wide-ranging RI detection (1.15 to 1.44), particularly in the n-IR band. The sensor presents two resonant peaks in visible band with maximum sensitivities of 4520 nm/RIU for C-2 and 1490 nm/RIU for C-1. While the maximum amplitude sensitivity is -168 RIU^{-1} for C-1 and -1093 RIU^{-1} for C-2. In contrast, in the n-IR band, the sensor presents a single peak with a maximum sensitivity of 1890 nm/RIU, although relatively low, enabling detection across a wider range of analytes. The dual operation in different spectral regimes and simultaneous detection of multi-analytes position the sensor as superior to others. Therefore, its suitability for practical applications is underscored by its high linearity, simple design, capacity for simultaneous multi-analyte sensing, and dynamic sensing range. The presented sensor holds promise for diverse and realistic applications in the field of RI sensing and multi-analyte detection.

References

[1] Yusuf Gamal, BM Younis, Mohamed Farhat O Hameed, and SSA Obayya. Plasmonic dual d-shaped pcf sensor for low refractive index applications. In *2022 International Conference on Numerical Simulation of Optoelectronic Devices (NUSOD)*, pages 193–194. IEEE, 2022.

[2] Iddrisu Danlard and Emmanuel Kofi Akowuah. Assaying with pcf-based spr refractive index biosensors: From recent configurations to outstanding detection limits. *Optical Fiber Technology*, 54:102083, 2020.

[3] Haoran Wang, Wen Zhang, Cancan Chen, Shoufeng Tang, and Hai Liu. A new methane sensor based on compound film-coated photonic crystal fiber and sagnac interferometer with higher sensitivity. *Results in Physics*, 15:102817, 2019.

[4] Emranul Haque, Abdullah Al Noman, and Feroz Ahmed. Numerical investigation of photonic crystal fiber-based biosensor for pathogens detection in water. *IEEE Access*, 10:88885–88893, 2022.

[5] Naseer Sabri, SA Aljunid, MS Salim, R Badlishah Ahmad, and Rosliha Kamaruddin. Toward optical sensors: Review and applications. In *Journal of Physics: Conference Series*, volume 423, page 012064. IOP Publishing, 2013.

[6] Malek G Daher, Naser M Ahmed, Osamah Alsalman, Abinash Panda, Ahmed Nabih Zaki Rashed, Juveriya Parmar, Sofyan A Taya, and Shobhit K Patel. Novel efficient surface plasmon resonance biosensor for the determination of sucrose concentration. *Plasmonics*, pages 1–7, 2023.

[7] Chao Liu, Jingwei Lü, Wei Liu, Famei Wang, and Paul K Chu. Overview of refractive index sensors comprising photonic crystal fibers based on the surface plasmon resonance effect. *Chinese Optics Letters*, 19(10):102202, 2021.

[8] Alireza Hassani and Maksim Skorobogatiy. Design of the microstructured optical fiber-based surface plasmon resonance sensors with enhanced microfluidics. *Optics express*, 14(24):11616–11621, 2006.

[9] Jianfei Liao, Junqiang Sun, Mingdi Du, and Yi Qin. Highly nonlinear dispersion-flattened slotted spiral photonic crystal fibers. *IEEE Photonics Technology Letters*, 26(4):380–383, 2013.

[10] Qiang Xu, Kang Li, Nigel Copner, and Shebao Lin. An ultrashort wavelength multi/demultiplexer via rectangular liquid-infiltrated dual-core polymer optical fiber. *Materials*, 12(10):1709, 2019.

[11] S Yogalakshmi, S Selvendran, and A Sivanantha Raja. Design and analysis of a photonic crystal fiber based polarization filter using surface plasmon resonance. *Laser Physics*, 26(5):056201, 2016.

[12] S Mohamed Nizar, S Rafi Ahamed, E Priyanka, R Jayasri, and B Kesavaraman. Comparison of different photonic crystal fiber structure: a review. In *Journal of Physics: Conference Series*, volume 1717, page 012048. IOP Publishing, 2021.

[13] Jitendra Narayan Dash and Rajan Jha. Graphene-based birefringent photonic crystal fiber sensor using surface plasmon resonance. *IEEE Photonics Technology Letters*, 26(11):1092–1095, 2014.

[14] Jonathan Boehm, Alexandre François, Heike Ebendorff-Heidepriem, and Tanya M Monro. Chemical deposition of silver for the fabrication of surface plasmon microstructured optical fibre sensors. *Plasmonics*, 6:133–136, 2011.

[15] Ying Lu, Xianchao Yang, Mintuo Wang, and Jianquan Yao. Surface plasmon resonance sensor based on hollow-core pcfs filled with silver nanowires. *Electronics Letters*, 51(21):1675–1677, 2015.

[16] Mohd Fahmi Azman, Ghafour Amouzad Mahdiraji, Wei Ru Wong, Rifat Ahmmed Aoni, and Faisal Rafiq Mahamd Adikan. Design and fabrication of copper-filled photonic crystal fiber based polarization filters. *Applied optics*, 58(8):2068–2075, 2019.

[17] Shaimaa I Azzam, Mohamed Farhat O Hameed, Rania Eid A Shehata, AM Heikal, and Salah SA Obayya. Multichannel photonic crystal fiber surface

plasmon resonance based sensor. *Optical and Quantum Electronics*, 48:1–11, 2016.

[18] Emranul Haque, Subaha Mahmuda, Md Anwar Hossain, Nguyen Hoang Hai, Yoshinori Namihira, and Feroz Ahmed. Highly sensitive dual-core pcf based plasmonic refractive index sensor for low refractive index detection. *IEEE photonics journal*, 11(5):1–9, 2019.

[19] Mohammad Al Mahfuz, Md Aslam Mollah, Moriom Rojy Momota, Alok Kumar Paul, Al Masud, Sanjida Akter, and Md Rabiul Hasan. Highly sensitive photonic crystal fiber plasmonic biosensor: Design and analysis. *Optical Materials*, 90:315–321, 2019.

[20] Mohammad Al Mahfuz, Md Anwar Hossain, Emranul Haque, Nguyen Hoang Hai, Yoshinori Namihira, and Feroz Ahmed. Dual-core photonic crystal fiber-based plasmonic ri sensor in the visible to near-ir operating band. *IEEE Sensors Journal*, 20(14):7692–7700, 2020.

[21] J Divya and S Selvendran. The impact of different background materials in a d-shaped photonic crystal fiber based plasmonic sensor: a comprehensive investigation. *Optical and Quantum Electronics*, 55(6):520, 2023.

[22] Honggang Pan, Fei Pan, Ailing Zhanga, Chuanbo Cao, and Fengjun Xue. Wide refractive index detection range surface plasmon resonance sensor based on d-shaped photonic crystal fiber. *Optical and Quantum Electronics*, 54(6):393, 2022.

[23] Emranul Haque, Md Anwar Hossain, Feroz Ahmed, and Yoshinori Namihira. Surface plasmon resonance sensor based on modified *d*-shaped photonic crystal fiber for wider range of refractive index detection. *IEEE Sensors Journal*, 18(20):8287–8293, 2018.

[24] Jianwei Wang, Chao Liu, Famei Wang, Weiquan Su, Lin Yang, Jingwei Lv, Guanglai Fu, Xianli Li, Qiang Liu, Tao Sun, et al. Surface plasmon resonance sensor based on coupling effects of dual photonic crystal fibers for low refractive indexes detection. *Results in physics*, 18:103240, 2020.

[25] Weiyou Zeng, Qinglan Wang, and Li Xu. Plasmonic refractive index sensor based on d-shaped photonic crystal fiber for wider range of refractive index detection. *Optik*, 223:165463, 2020.

[26] Tanvir Alam Roni, Rifat Hassan, and Mohammad Faisal. Dual-side polished spr biosensor with wide sensing range. In *2020 11th International Conference on Electrical and Computer Engineering (ICECE)*, pages 487–490. IEEE, 2020.

[27] Gongli Xiao, Jiapeng Su, Hongyan Yang, Zetao Ou, Haiou Li, Xingpeng Liu, Zanhui Chen, Yunhan Luo, and Jianqing Li. Fiber optic sensor with a gold nanowire group array for broad range and low refractive index detection. In *Photonics*, volume 9, page 661. MDPI, 2022.

[28] Firoz Haider, Md Mashrafi, Rifat Ahmmed Aoni, Rakib Haider, Moqbull Hossen, Tanvir Ahmed, Ghafour Amouzad Mahdiraji, and Rajib Ahmed. Multi-analyte detection based on integrated internal and external sensing approach. *IEEE Transactions on NanoBioscience*, 21(1):29–36, 2021.

[29] QM Kamrunnahar, Firoz Haider, Rifat Ahmmed Aoni, Jannatul Robaiat Mou, Shamsuttiyeba Shifa, Feroza Begum, Hairul Azhar Abdul-Rashid, and Rajib Ahmed. Plasmonic micro-channel assisted photonic crystal fiber based highly sensitive sensor for multi-analyte detection. *Nanomaterials*, 12(9):1444, 2022.

[30] Farhan Mumtaz, Bohong Zhang, Muhammad Roman, Lashari Ghulam Abbas, Muhammad Aqueel Ashraf, and Yutang Dai. Computational study: Windmill-shaped multi-channel spr sensor for simultaneous detection of multi-analyte. *Measurement*, 207:112386, 2023.

[31] Shivam Singh, Bhargavi Chaudhary, Anurag Upadhyay, Divya Sharma, N Ayyanar, and Sofyan A Taya. A review on various sensing prospects of spr based photonic crystal fibers. *Photonics and Nanostructures-Fundamentals and Applications*, page 101119, 2023.

[32] Fengmin Wang, Yong Wei, and Yanhong Han. High sensitivity and wide range refractive index sensor based on surface plasmon resonance photonic crystal fiber. *Sensors*, 23(14):6617, 2023.

[33] Hicham El Hamzaoui, Youcef Ouerdane, Laurent Bigot, Géraud Bouwmans, Bruno Capoen, Aziz Boukenter, Sylvain Girard, and Mohamed Bouazaoui. Sol-gel derived ionic copper-doped microstructured optical fiber: a potential selective ultraviolet radiation dosimeter. *Optics express*, 20(28):29751–29760, 2012.

[34] Guillaume Vienne, Yong Xu, Christian Jakobsen, Hans-Jürgen Deyerl, Jesper B Jensen, Thorkild Sørensen, Theis P Hansen, Yanyi Huang, Matthew

Terrel, Reginald K Lee, et al. Ultra-large bandwidth hollow-core guiding in all-silica bragg fibers with nano-supports. *Optics Express*, 12(15):3500–3508, 2004.

[35] Andrea Bertoncini and Carlo Liberale. 3d printed waveguides based on photonic crystal fiber designs for complex fiber-end photonic devices. *Optica*, 7(11):1487–1494, 2020.

[36] S Selvendran, A Sivanantharaja, and S Yogalakshmi. A highly sensitive bezier polygonal hollow core photonic crystal fiber biosensor based on surface plasmon resonance. *Optik*, 171:109–113, 2018.

[37] Moutusi De, Tarun Kumar Gangopadhyay, and Vinod Kumar Singh. Prospects of photonic crystal fiber as physical sensor: An overview. *Sensors*, 19(3):464, 2019.

[38] Veerpal Kaur and Surinder Singh. Design approach of solid-core photonic crystal fiber sensor with sensing ring for blood component detection. *Journal of Nanophotonics*, 13(2):026011–026011, 2019.

[39] Arati Shah and Rajesh Kumar. *A Review on Photonic Crystal Fibers*, pages 1241–1249. 01 2020.

[40] Ahmmed A Rifat, Rajib Ahmed, G Amouzad Mahdiraji, and FR Mahamd Adikan. Highly sensitive d-shaped photonic crystal fiber-based plasmonic biosensor in visible to near-ir. *IEEE Sensors Journal*, 17(9):2776–2783, 2017.

[41] Nazmus Sakib, Sumaya Arafin, Zayed Anis, Walid Hassan, Thouhidur Rahman, and Tazin Fatema. Design and analysis of a highly sensitive modified square structure dual slotted single core plasmonic biosensor. *Optics Continuum*, 1(2):143–160, 2022.

[42] Jiapeng Su, Gongli Xiao, Hongyan Yang, Jiayu Chen, Haiou Li, Xingpeng Liu, Yunhan Luo, and Jianqing Li. Highly sensitive multi-channel biosensor for low-interference simultaneous detection. *Nanomaterials*, 13(2):246, 2023.

[43] Zhiyong Yin, Xili Jing, Ge Bai, Chun Wang, Chaoyi Liu, Zhigang Gao, and Kaifeng Li. A broadband spr dual-channel sensor based on a pcf coated with sodium-silver for refractive index and temperature measurement. *Results in Physics*, 41:105943, 2022.

[44] RongQiu Mu, Hongdan Wan, WeiHua Shi, Huan Liang, and Yue Lou. Design and theoretical analysis of high-sensitive surface plasmon resonance sensor based on au/ti 3 c 2 tx-mxene hybrid layered d-shaped photonic crystal fiber. *IEEE Sensors Journal*, 2023.

[45] Farhan Mumtaz, Muhammad Roman, Bohong Zhang, Lashari Ghulam Abbas, Yutang Dai, Muhammad Aqueel Ashraf, Muhammad Arshad Fiaz, and Amit Kumar. Mxene (ti3c2tx) coated highly-sensitive d-shaped photonic crystal fiber based spr-biosensor. *Photonics and Nanostructures-Fundamentals and Applications*, 52:101090, 2022.

[46] Nasir Mahmood Anjum, Farhan Mumtaz, and Muhammad Aqueel Ashraf. Design and analysis of gold-nanowires based multi-channel spr sensor. *Results in Optics*, 11:100397, 2023.

[47] Farhan Mumtaz. Detection of critical cancer cells in human organs using dual demodulation photonic crystal fiber: Numerical study. *Results in Optics*, 12:100493, 2023.

[48] Ahmet Yasli, Huseyin Ademgil, Shyqyri Haxha, and Amar Aggoun. Multi-channel photonic crystal fiber based surface plasmon resonance sensor for multi-analyte sensing. *IEEE Photonics Journal*, 12(1):1–15, 2019.